VERUSCRIPT

VERUSCRIPT FUNCTIONAL NANOMATERIALS
www.veruscript.com/fnan

Multilayered graphene/$ZnFe_2O_4$ hybrid composite: Rational preparation, characterization and superior adsorption of Congo red

Original article

Article history:
Received: 8 September 2016
Accepted: 8 December 2016
Published: 18 May 2017

Check for updates

***Correspondence:**
baoping.jia@cczu.edu.cn
zhangwei811017@hotmail.com
†QW and BJ contributed equally to this work

Peer review:
Double blind

Keywords:
graphene; hybrid; Congo red; multilayer; nanocomposite

Citation:
Wang Q., Jia B., Zhang W., Liu H., Min X., and Ding J. Multilayered graphene/$ZnFe_2O_4$ hybrid composite: Rational preparation, characterization and superior adsorption of Congo red. Veruscript Functional Nanomaterials. 2017; 1: #12RZVF. https://doi.org/10.22261/12RZVF

Qiuze Wang[1,†], Baoping Jia[1,2,*,†], Wei Zhang[3,4,*], Hui Liu[5], Xiaobo Min[5], Jianning Ding[1]

[1] *School of Materials Science and Engineering, Changzhou University, Changzhou, Jiangsu 213164, China*
[2] *Jiangnan Graphene Research Institute, Changzhou, Jiangsu 213149, China*
[3] *Department of Urban Engineering, University of Tokyo, 113-0033, Japan*
[4] *School of Natural and Built Eniveronments, University of South Australia, SA 5095, Australia*
[5] *School of Metallurgy and Environment, National Engineering Research Center for Control & Treatment of Heavy Metal Pollution, Central South University, Changsha, China*

Abstract

Multilayered porous hierarchical structure of graphene/$ZnFe_2O_4$ hybrids was prepared via in situ hydrothermal growth of $ZnFe_2O_4$ nanocrystals within interlayer space of reduced graphene oxide, which demonstrated a high specific area of 117 $m^2 \cdot g^{-1}$ and rational porous structures. Batch adsorption studies showed that the product possesses superior adsorption capacity of dyes such as Congo red from aqueous solution. Adsorption equilibrium and kinetic analysis indicated that the adsorption isotherm was well fitted by Langmuir isothermal model with the maximum adsorption capacity of 404.12 $mg \cdot g^{-1}$, and the adsorption kinetics followed the pseudo-second-order kinetic equation. Furthermore, this new product can be magnetically separated and regenerated easily, presenting an effective adsorbent for wastewater purification.

Introduction

Increasing compositional and structural complexity of materials has been recognized as one of the most important strategies in the field of material chemistry, for the expanded material functionality that could benefit a wide scope of applications. Specific to nanomaterials, this principle has led to considerable research efforts in the development of novel hybrid/functional nanostructures, which increases the impact of nanotechnology on semiconductor electronics [1], medicine [2], catalysis [3–6], energy generation/storage [7,8] and sensors [9]. In any case of constructing complex nano-

OPEN ACCESS

structures, challenges exist in the controlling of composition, morphology and structure of different nanoscale building blocks, as well as in the precise placement of these building blocks during rational assembly.

In the past decade, graphene-based hierarchical structures composed by nanoscale building blocks have emerged as a new class of hybrid materials due to the designable structure [10,11] coupled with other building blocks, including polymers [12], metal and metal oxide nanostructures [13]. Existing methods to synthesize graphene-based hybrids include layer-by-layer assembling of oppositely charged reduced graphene oxide (rGO) and guest counterpart [14], simple blending of graphene with other nanocomponents [15–17], as well as growing functional nanostructures over rGO nanosheets [18].

A particularly attractive application of this kind of hybrids is to develop a new class of adsorbent with high adsorption and facile separation capacity for water purification [19]. In this context, it is critical to design, controllably synthesize and tailor the hierarchical nanostructures to obtain desirable pore network. According to previous reports, graphene or graphene oxide–related hierarchical nanostructures could be achieved with various approaches [20–25]. Among those, template-free hydrothermal/solvothermal routes are more recommendable due to their simple operation procedures and easily adjustable process parameters simultaneously. Previous studies have reported that typical building blocks such as nanoparticles, nanorods, nanosheets and so on can achieve structures varying largely in morphologies from spheres, hollow spheres to flower-like structures, and so on [26–28]. Though tremendous progress has been made in this field, how to fabricate effective large-scale hierarchical self-assembly of some functional materials is still a challenge to material scientists.

In this study, a new class of multilayered hierarchical structure of rGO/$ZnFe_2O_4$ hybrid adsorbents was synthesized via in situ hydrothermal growth of $ZnFe_2O_4$ nanocrystals within interlayer space of rGO, which exhibit excellent adsorption capability of Congo red (CR) and potential recyclability.

Experimental

Synthesis of porous hierarchical rGO/$ZnFe_2O_4$ nanostructures

All reagents used were of analytical grade and were used as received without further purification. rGO was purchased from the Sixth Element Carbon, Changzhou, China. In a typical procedure, 0.05 g of rGO was ultrasonicated in 40 mL of deionized water for 1 h to obtain homogenous solution I. Then, 10 mmol of $ZnSO_4{\cdot}7H_2O$ and 20 mmol of $FeSO_4$ (Fe:Zn=2:1) were placed into the above solution, which was magnetically stirred for 1 h to form a transparent solution II at room temperature. Then, the solutions I and II were mixed to form solution III, and then 30 mL of $H_2C_2O_4$ (30 mmol) aqueous solution was slowly dropped into the solution III to form the final solution IV (rGO/$ZnFe_2(C_2O_4)3$). Then the mixed solution IV was transferred to a hydrothermal synthesis reactor and kept at 120°C for 24 h (rGO/$ZnFe_2O_4$). The resulting solids were filtered from the suspension, washed with deionized water and dried at 100°C. Finally, the solid was calcined in air at 400°C (heating rate 1°C min^{-1}) for 2 h.

Material characterization

Field emission scanning electron microscope (SEM, XL30ESEM-FEG) was used for morphological characterization of the rGO/$ZnFe_2O_4$. The crystalline phase of the as-prepared samples was investigated by X-ray powder diffraction (XRD) using a D8 advance X-ray diffractometer with Cu Kα radiation operating at 40 kV and 200 mA. Measurement of the specific surface area and analysis of the porosity for the rGO/$ZnFe_2O_4$ product were carried out through measuring N_2 adsorption −desorption isotherms at 77 K with a Quantachrome NOVA-3000 system. The absorbance of the solutions was analyzed by a UV–Vis spectrophotometer (Model 721, Shanghai Precision & Scientific Instrument Co., Ltd., China).

Evaluation of adsorption performance

Typically, a stock solution of CR (1000 mg L^{-1}) was prepared using Ultrapure@ water, and then the reaction solutions with different initial concentrations (20–800 mg·L^{-1}) were obtained by successive dilutions. Adsorption experiments were performed by adding 0.02 g of as-obtained porous hierarchical rGO/$ZnFe_2O_4$ into various initial CR aqueous solutions, and then the solutions were put in an air bath thermostatic rotary shaker (shaken at 120 rpm) at various temperatures and natural pH. At the end of the adsorption process, the concentrations of the CR solutions were analyzed by using ascorbic acid method to monitor the absorbance at 518 nm with a spectrophotometer. The adsorption capacity, q_e (mg·g^{-1}), was calculated using the following equation [29]:

$$q_e = (C_0 - C_e)V/W \quad (1)$$

where C_0 is the initial concentration of CR (mg·L^{-1}), C_e is the equilibrium concentration of CR after adsorption (mg·L^{-1}), V is the volume of CR solution (mL) and W is the weight of the synthesized adsorbent (mg).

The kinetics of adsorption was determined by adding rGO/$ZnFe_2O_4$ sample (20 mg) into 50.0 mL of the CR solution (50 mg·L^{-1}). The isotherm for the adsorption of CR on rGO/$ZnFe_2O_4$ was performed by adding 20 mg of the rGO/$ZnFe_2O_4$ sample into 50 mL of the CR solution with various concentrations (20, 50, 100, 200, 300, 400, 500 and 800 mg L^{-1}). The adsorption capacity was evaluated on the basis of a mass balance between the initial and the immediate or final CR concentrations.

Results and discussion

XRD patterns

The crystal phase of the as-prepared samples was investigated by XRD technique. XRD pattern (a) in Figure 1 confirmed the formation of Zinc ferrite (JCPDS, No. 380430). The characteristic diffraction peaks at 2θ = 18.8°, 29.7°, 35.2°, 42.3°, 53.7°, 56.4° and 62.1° represent the corresponding indexes (111), (220), (311), (400), (422), (511) and (440), respectively. When compared with the parent $ZnFe_2O_4$ peak, the peak of rGO/$ZnFe_2O_4$ was found to be similar, except for the typical small peak around 25°, and this was attributed to the rGO inside, which can be confirmed by SEM morphology picture.

Structure characterization of the porous hierarchical rGO/$ZnFe_2O_4$ nanostructures

The morphology and microstructure of rGO, $ZnFe_2O_4$ and as-obtained rGO/$ZnFe_2O_4$ composite were investigated using SEM. Figure 2a shows the rGO. It can be seen that the structure consists of stacking layers, and the layers overlap closely. The surface is full of crumples like waves, and there are also part of the reunion and secondary accumulation. The $ZnFe_2O_4$ in Figure 2b exhibits a regular rod-like hierarchical nanostructure self-assembled by nanorods. The detailed morphology of the hierarchical nanostructure is shown in the top left corner, from which we can see that the fuzzy nanorod ends are composed of large amounts of nanorods across the entire bowknot. The morphology and microstructure of as-obtained rGO/$ZnFe_2O_4$ composite are shown in Figure 2c. It is observed that the characteristic structure of rGO was destroyed and self-assembled into a regular multitude nanostructure with several stacking layers. This indicated that the additional $ZnFe_2O_4$ mixed well with rGO, and there were also well-defined pore structures present in it. Under higher magnification, naked rGO sheets of smaller scale were clearly spotted in the surface layer.

On the basis of these results, the morphogenesis of rGO/$ZnFe_2O_4$ hierarchical architectures cannot be simply ascribed to the formation of the macroscopic structure via the physical process of rGO and $ZnFe_2O_4$ blending, which was contributed neither by nanosheets nor by rod-like multilayers. During the hydrothermal reaction (Figure 3), $ZnFe_2O_4$ played an important role in the growth of hybrid composite because of the interaction of $ZnFe_2O_4$ with the surface of graphene, where a small amount

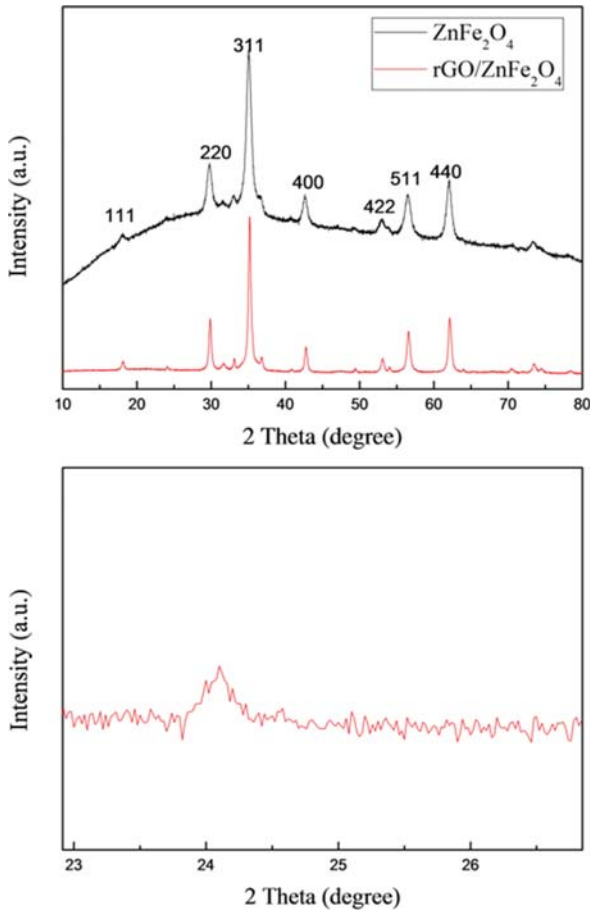

Figure 1. XRD pattern of $ZnFe_2O_4$, rGO/$ZnFe_2O_4$ and rGO samples.

of functional group existed after its reduction [30]. Under electrostatic attraction, the presence of these functional groups can position the $ZnFe_2O_4$ crystal nucleus, which can inhibit the growth of rGO aggregation in the process of $ZnFe_2O_4$ crystallization and, thus, lead to a high specific surface area of hybrid composite.

N_2 adsorption–desorption measurement

Figure 4a and 4b presents the N_2 adsorption–desorption isotherm and the pore size distribution of the materials. As shown in Figure 4a, the isotherm of the sample exhibited type IV isotherm with a type H3 hysteresis loop, according to the de Boer's classification [31]. There was the distinct hysteresis loop in the P/P_0 range of 0.8–1.0 because of capillary condensation, and multilayer adsorption indicated the mesoporous characteristics of the sample. The Brunauer, Emmett and Teller surface area of the particles was estimated to be 177 $m^2 \cdot g^{-1}$. High surface area was probably because the $ZnFe_2O_4$ can effectively decrease the aggregation of the rGO layers (since the strong van der Waals interactions among these reduced graphene sheets could result in aggregation) [32]. Pore size distribution was calculated by the Barrett, Joyner and Halenda method using desorption branches (Figure 4b). Total pore volume and average pore diameter were estimated to be 0.35 cm^3 g^{-1} and 49 nm.

The adsorption of Congo red onto rGO/$ZnFe_2O_4$

Adsorption kinetics

Generally, if materials possess porous hierarchical structures and high surface area, it would possess more available active adsorption sites and efficient transport pathways and might exhibit excellent

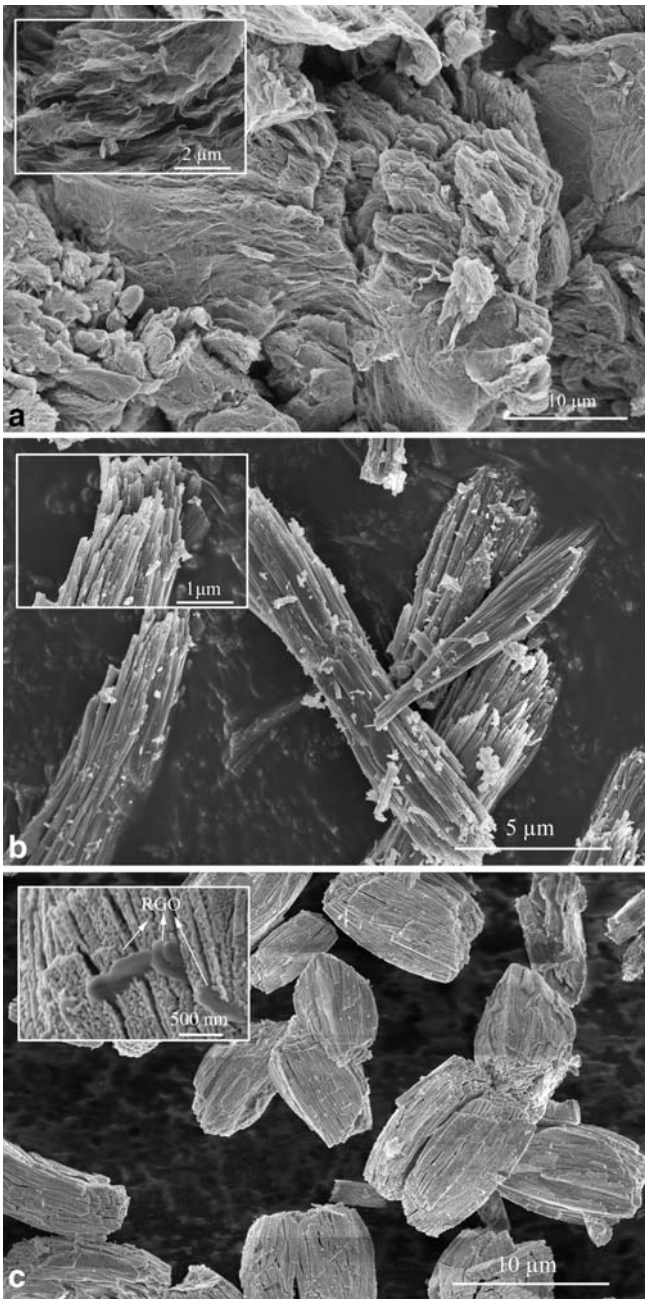

Figure 2. SEM images of rGO (a), $ZnFe_2O_4$ (b) and rGO/$ZnFe_2O_4$ (c), with each inset featuring increased magnification.

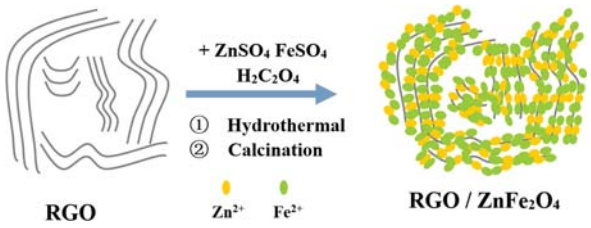

Figure 3. Schematics of the synthesis procedure for rGO/$ZnFe_2O_4$ hybrid composites.

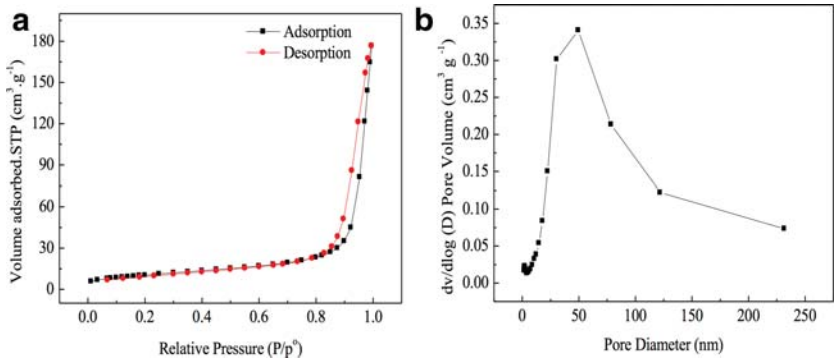

Figure 4. (a) N_2 adsorption/desorption isotherms of rGO/$ZnFe_2O_4$ and (b) pore size distributions calculated from the N_2 desorption isotherms according to the BJH model.

adsorption performance [33]. Herein, the kinetic curves for CR removal at 298, 308 and 318 K from aqueous solutions with fixed initial CR concentration of 50 mg·L^{-1} onto composite (0.02 g) are shown in Figure 5a. For CR removal from solution at all three temperatures, it can be seen that adsorption capacity increased sharply in the initial stage and then tended to gradually reach adsorption equilibrium in about 40 min. This is probably due to the decreasing solution concentration and the exhaustion of the adsorption sites with the adsorption time. A further increase in temperature from 298 to 318 K only resulted in a slight increase in the equilibrium CR adsorption from 118.19 to 119.03 mg·g^{-1}.

To evaluate the adsorption kinetic process, various kinetic models, such as pseudo-first-order kinetic model [34] and pseudo-second-order model [35], were used to examine the diffusion mechanism involved during the adsorption process. The experimental kinetic data were fitted to the following two typical kinetic equations to provide a better understanding of the CR sorption process in rGO/$ZnFe_2O_4$, where K_1 (L min^{-1}) is the rate constant of pseudo-first-order adsorption; q_e and q_t (mg·g^{-1}) denote the amounts of contaminant adsorbed at equilibrium and at time (t), respectively. K_2 (mg·g^{-1} min^{-1}) is the rate constant of pseudo-second-order adsorption. The kinetic parameters for the adsorption kinetic models are summarized in Table 1. The fitting results of the experimental data to the models are shown in Figure 5c and 5d. For the pseudo-second-order kinetic model, the R^2 values were found to be higher than 0.99, and the calculated q_e values ($q_{e,\ cal}$) were found to agree very well with the values of experimental data ($q_{e,\ exp}$), which indicated that the pseudo-second-order kinetic model provided the best correlation for all of the adsorption process. The adsorption process was well presented in Figure 5b. The solution color decreased lightly with increasing time, and it became colorless and transparent in 40 min.

$$\text{Pseudo-first-order equation } \ln q_e = \ln(q_e - q_t) - K_1 t/2.303 \quad (2)$$

$$\text{Pseudo-second-order equation } t/q_t = 1/(K_2 q_e^{\ 2}) + t/q_e \quad (3)$$

Adsorption isotherm

The adsorption isotherm curves of CR removal at 298, 308 and 318 K from aqueous solutions onto mesoporous rGO/$ZnFe_2O_4$ are shown in Figure 6a. The adsorption isotherm studies in different temperature were carried out to determine the rate of CR removal from solution by rGO/$ZnFe_2O_4$. As shown in Figure 6a, the adsorption equilibrium capacity was found to increase with increasing temperature. The equilibrium CR adsorption capacity was found to be 358.76, 379.38 and 404.12 mg·g^{-1}, respectively, with different temperatures at 298, 308 and 318 K, indicating that the as-prepared mesoporous rGO/$ZnFe_2O_4$ can be used as a potential adsorbent for the removal of CR. More importantly, the mesoporous rGO/$ZnFe_2O_4$ can be magnetically separated from the solution containing CR.

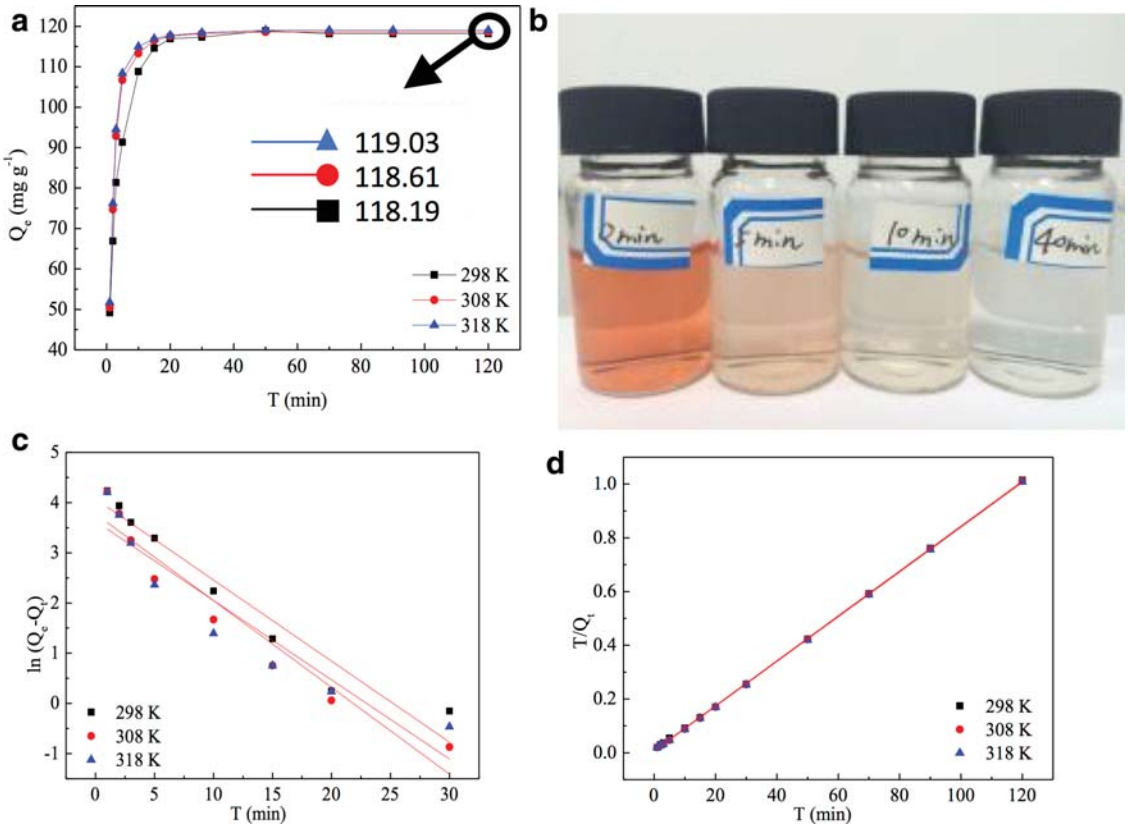

Figure 5. (a) Effect of contact time on the adsorption kinetics of CR (50 mL, 50 mg·L^{-1}); (b) Pictures of absorption of CR after different periods of time; (c) Pseudo-first-order plots; (d) pseudo-second-order kinetics.

Table 1. Kinetic constants for CR removal onto mesoporous rGO/$ZnFe_2O_4$.

Temp	Pseudo-first-order			Pseudo-second-order		
	K_1	q_e	R^2	K_2	q_e	R^2
298 K	−0.16151	4.07250	0.93911	0.0076547	120.48	0.99988
308 K	−0.17192	3.77751	0.93151	0.011677	120.48	0.99990
318 K	−0.15797	3.62974	0.87950	0.012302	120.48	0.99993

The Langmuir [36] and Freundlich [37] isotherm equations are widely used to describe the sorption processes in sorption experiments. The linear form of the isotherm equations expressed in Eqs. (4) and (5) was used for modeling these adsorption isotherm data, where C_e (mg·L^{-1}) and q_e (mg·g^{-1}) are the equilibrium adsorbate concentrations in the aqueous and solid phases; q_m (mg·g^{-1}) is the maximum adsorption capacity, and b is the binding constant, which is relate to the heat of Langmuir adsorption; K_f is the Freundlich equilibrium constant, indicative of adsorption capacity, and $1/n$ is the Freundlich adsorption constant, the reciprocal of which is indicative of adsorption intensity.

$$C_e/q_e = C_e/q_m + 1/K_L q_e \quad (4)$$

$$\ln q_e = \ln K_f + 1/n \ln C_e \quad (5)$$

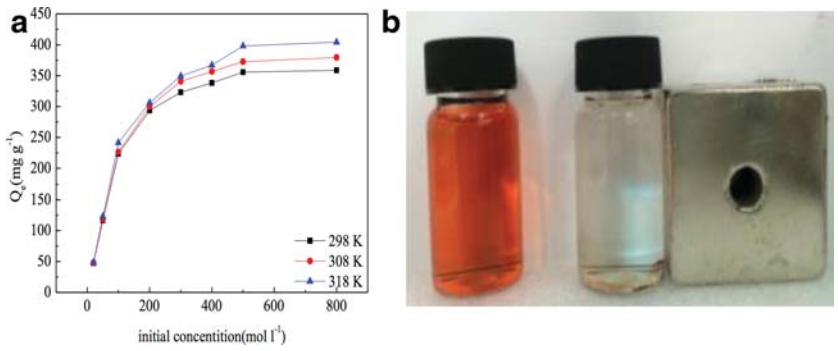

Figure 6. (a) Effect of initial concentration on the adsorption of phosphate in 50 mL solution at natural 3.0. (b) Photos of initial CR (50 mg·L^{-1}) aqueous solution treated by the rGO/$ZnFe_2O_4$ after 2 h.

Table 2. Values of Langmuir and Freundlich constants for adsorption of phosphate onto mesoporous rGO/$ZnFe_2O_4$.

Temp	Langmuir			Freundlich		
	Q_L	K_L	R^2	K_F	n	R^2
25	347.22	0.1505	0.99926	73.57	3.57	0.8259
35	361.01	0.1760	0.99915	1.7994	3.57	0.85108
45	371.75	0.5886	0.9971	108.5	4.41	0.82709

Fitted constants for the Langmuir and Freundlich isotherm models along with regression coefficients (R^2) are summarized in Table 2. The R^2 values obtained for Langmuir isotherms were higher than those for Freundlich isotherm, indicating that the Langmuir adsorption model was more suitable to describe the adsorption process. The maximum adsorption capacity of the porous hierarchical rGO/$ZnFe_2O_4$ for CR was calculated to be 404.12 mg·g^{-1}. This ultrahigh removal efficiency could be largely attributed to the highly porous structure and large surface area of the spheres, as well as the electrostatic attraction between the rGO/$ZnFe_2O_4$ surfaces and CR. Table 3 shows the adsorption capacities of the hollow nest-like α-Fe_2O_3 spheres and those of some previously reported materials. It appeared that the adsorption capacity of the as-prepared rGO/$ZnFe_2O_4$ composite for CR was much higher than that for the majority of various adsorbents reported in the references.

Conclusion

In this study, a magnetically separable adsorbent rGO/$ZnFe_2O_4$ with multilayered porous hierarchical structure has been synthesized via in situ reduction of rGO in the presence of $ZnFe_2(C_2O_4)_3$ and sequential calcinations. The as-prepared nanocomposites were demonstrated to possess superior specific area (117 m^2·g^{-1}) of rational porous structures. In batch adsorption studies, the composite revealed efficient adsorption capacity of Congo red from aqueous solution. Adsorption equilibrium and kinetic experiments indicated that the adsorption isotherm data were well fitted by Langmuir isothermal model with the maximum adsorption capacity of 404.12 mg·g^{-1}, and the adsorption kinetics follows the pseudo-second-order kinetic equation. Furthermore, the used materials can be magnetically separated and regenerated. The as-prepared multilayered porous rGO/$ZnFe_2O_4$ hybrid composite has proved to be a promising adsorbent for effective removal of Congo red from wastewater.

Table 3. BET surface area and the maximum Congo red removal capacity of various adsorbents.

Adsorbent sample	BET surface area ($m^2 \cdot g^{-1}$)	Maximum adsorption capacity ($mg \cdot g^{-1}$)	Reference
Porous hierarchical rGO/$ZnFe_2O_4$	177	404.12	This study
Hollow nest-like α-Fe_2O_3 spheres	152.45	160	[38]
Hierarchical spindle-like r-Al_2O_3	149	90	[39]
Graphene oxide/chitosan/silica fibers	–	294.12	[40]
Flower-like MgO	–	72	[41]
Hierarchical hollow structure ZnO	31	97	[42]

Funding sources

This work was supported by National Natural Science Foundation of China (21301021), Natural Science Foundation of Jiangsu Province (BK20130254), Jiangsu Province Science and Technology Support Project (BC2015071) and Open Topic funding of National Engineering Research Center for Control & Treatment of Heavy Metal Pollution.

Competing interests

Baoping Jia, Qiuze Wang, Wei Zhang, Hui Liu, Xiaobo Min and Jianning Ding declare that they have no conflict of interest.

References

1. Ameer S., Gul I. H., Mahmood N., and Mujahid M. Semiconductor-to-metallic flipping in a $ZnFe_2O_4$–graphene based smart nano-system: temperature/microwave magneto-dielectric spectroscopy. Materials Characterization. 2015; 99: 254–265. https://doi.org/10.1016/j.matchar.2014.11.018.

2. Bragg A., Khosravi F., King B., Rai S. N., Kloecker G., et al. Nanotube-and graphene-based photomedicine for cancer. Applications of Nanoscience in Photomedicine. 2015: 291. https://doi.org/10.1533/9781908818782.291.

3. Shi P., Su R., Wan F., Zhu M., Li D., et al. Synergistic catalysis of Co_3O_4 and graphene oxide on Co_3O_4/GO catalysts for degradation of Orange II in water by advanced oxidation technology based on sulfate radicals. Chemical Engineering Journal. 2014; 240: 264–270. https://doi.org/10.1016/j.cej.2013.11.089.

4. Li H., Zhang W., Zou L., Pan L., and Sun Z. Synthesis of TiO_2–graphene composites via visible-light photocatalytic reduction of graphene oxide. Journal of Materials Research. 2011; 26 (08): 970–973. https://doi.org/10.1557/jmr.2011.22.

5. Zhang W. and Jia B. Toward anti-fouling capacitive deionization by using visible-light reduced TiO_2/graphene nano-composites. MRS Communications. 2015; 5 (04): 613–617. https://doi.org/10.1557/mrc.2015.65.

6. Jia W., Wu X., Jia B., Qu F., and Jin Fan H. Self-assembled porous ZnS nanospheres with high photocatalytic performance. Science of Advanced Materials. 2013; 5 (10): 1329–1336. https://doi.org/10.1166/sam.2013.1593.

7. Jeong H., Kim B., Higgins M., and Wallace G. Highly stretchable reduced graphene oxide (rGO)/single-walled carbon nanotubes (SWNTs) electrodes for energy storage devices. Electrochimica Acta. 2015; 163: 149–160. https://doi.org/10.1016/j.electacta.2015.02.022.

8. Jia B., Wang Q., Zhang W., Lin B., Yuan N., et al. A new oil/water interfacial assembly of sulphonated graphene into ultrathin films. RSC Advances. 2014; 4 (65): 34566–34571. https://doi.org/10.1039/C4RA05160B.

9. Inyawilert K., Wisitsoraat A., Sriprachaubwong C., Tuantranont A., Phanichphant S., et al. Rapid ethanol sensor based on electrolytically-exfoliated graphene-loaded flame-made In-doped SnO_2 composite film. Sensors and Actuators B: Chemical. 2015; 209: 40–55. https://doi.org/10.1016/j.snb.2014.11.086.

10. Fang Q., Shen Y., and Chen B. Synthesis, decoration and properties of three-dimensional graphene-based macrostructures: A review. Chemical Engineering Journal. 2015; 264: 753–771. https://doi.org/10.1016/j.cej.2014.12.001.

11. Ma L., Zhou X., Xu L., Xu X., Zhang L., et al. Ultrathin few-layered molybdenum selenide/graphene hybrid with superior electrochemical Li-storage performance. Journal of Power Sources. 2015; 285: 274–280. https://doi.org/10.1016/j.jpowsour.2015.03.120.

12. Hu K., Kulkarni D. D., Choi I., and Tsukruk V. V. Graphene-polymer nanocomposites for structural and functional applications. Progress in Polymer Science. 2014; 39 (11): 1934–1972. https://doi.org/10.1016/j.progpolymsci.2014.03.001.

13. Wu Z.-S., Zhou G., Yin L. C., Ren W., Li F., et al. Graphene/metal oxide composite electrode materials for energy storage. Nano Energy. 2012; 1 (1): 107–131. https://doi.org/10.1016/j.nanoen.2011.11.001.

14. Hong T.-K., Dong W. L., Choi H. J., Shin H. S., and Kim B. S. Transparent, flexible conducting hybrid multilayer thin films of multiwalled carbon nanotubes with graphene nanosheets. Acs Nano. 2010; 4 (7): 3861–3868. https://doi.org/10.1021/nn100897g.

15. Yoo E., Kim J., Hosono E., Zhou H., Kudo T., et al. Large reversible Li storage of graphene nanosheet families for use in rechargeable lithium ion batteries. Nano letters. 2008; 8 (8): 2277–2282. https://doi.org/10.1021/nl800957b.

16. Tung V. C., Chen L. M., Allen M. J., Wassei J. K., Nelson K., et al. Low-temperature solution processing of graphene–carbon nanotube hybrid materials for high-performance transparent conductors. Nano letters. 2009; 9 (5): 1949–1955. https://doi.org/10.1021/nl9001525.

17. King P. J., Khan U., Lotya M., De S., and Coleman J. N. Improvement of transparent conducting nanotube films by addition of small quantities of graphene. Acs Nano. 2010; 4 (7): 4238–4246. https://doi.org/10.1021/nn100542z.

18. Fan Z., Yan J., Zhi L., Zhang Q., Wei T., et al. A Three-Dimensional Carbon Nanotube/Graphene Sandwich and Its Application as Electrode in Supercapacitors. Advanced materials. 2010; 22 (33): 3723–3728. https://doi.org/10.1002/adma.201001029.

19. Chella S., Kollu P., Komarala E. V. P. R., Doshi S., Saranya M., et al. Solvothermal synthesis of $MnFe_2O_4$-graphene composite—Investigation of its adsorption and antimicrobial properties. Applied Surface Science. 2015; 327: 27–36. https://doi.org/10.1016/j.apsusc.2014.11.096.

20. Chi C., Xu H., Zhang K., Wang Y., Zhang S., et al. 3D hierarchical porous graphene aerogels for highly improved adsorption and recycled capacity. Materials Science and Engineering: B. 2015; 194: 62–67. https://doi.org/10.1016/j.mseb.2014.12.026.

21. Lingappan N., Van N. H., Lee S., and Kang D. J. Growth of three dimensional flower-like molybdenum disulfide hierarchical structures on graphene/carbon nanotube network: an advanced heterostructure for energy storage devices. Journal of Power Sources. 2015; 280: 39–46. https://doi.org/10.1016/j.jpowsour.2015.01.064.

22. Sun F., Huang K., Qi X., Gao T., Liu Y., et al. Enhanced 3D hierarchical double porous Co_3O_4/graphene architecture for superior rechargeable lithium ion battery. Ceramics International. 2014; 40 (1): 2523–2528. https://doi.org/10.1016/j.ceramint.2013.07.096.

23. Xu J., Dang D. K., Jin S. C., Hur S. H., Choi W. M., et al. Sonochemical fabrication of Cu_2O@C/graphene nanohybrid with a hierarchical architecture. Journal of Solid State Chemistry. 2014; 220: 111–117. https://doi.org/10.1016/j.jssc.2014.08.017.

24. Meidanchi A. and Akhavan O. Superparamagnetic zinc ferrite spinel–graphene nanostructures for fast wastewater purification. Carbon. 2014; 69: 230–238. https://doi.org/10.1016/j.carbon.2013.12.019.

25. Yu Z., Wu X., Wang J., Jia W., Zhu G., et al. Facile template-free synthesis and visible-light driven photocatalytic performances of dendritic CdS hierarchical structures. Dalton Transactions. 2013; 42 (13): 4633–4638. https://doi.org/10.1039/c2dt32486e.

26. Jia Z., Liu J., Wang Q., Ye M., and Zhu R. Facile preparation of mesoporous nickel oxide microspheres and their adsorption property for methyl orange from aqueous solution. Materials Science in Semiconductor Processing. 2014; 26: 716–725. https://doi.org/10.1016/j.mssp.2014.06.026.

27. Wang L., Huang Y., Li C., Chen J., and Sun X. Hierarchical composites of polyaniline nanorod arrays covalently-grafted on the surfaces of graphene@Fe_3O_4@C with high microwave absorption performance. Composites Science and Technology. 2015; 108: 1–8. https://doi.org/10.1016/j.compscitech.2014.12.011.

28. Jia Z., Yang L., Wang Q., Liu J., Ye M., et al. Synthesis of hierarchical $CoFe_2O_4$ nanorod-assembled superstructures and its catalytic application. Materials Chemistry and Physics. 2014; 145 (1): 116–124. https://doi.org/10.1016/j.matchemphys.2014.01.048.

29. Hameed B. Equilibrium and kinetic studies of methyl violet sorption by agricultural waste. Journal of Hazardous Materials. 2008; 154 (1): 204–212. https://doi.org/10.1016/j.jhazmat.2007.10.010.

30. Hsiao M.-C., Liao S.-H., Yen M.-Y., Liu P., Pu N.-W., et al. Preparation of covalently functionalized graphene using residual oxygen-containing functional groups. ACS applied materials & interfaces. 2010; 2 (11): 3092–3099. https://doi.org/10.1021/am100597d.

31. Yang S., Liang G., Gu A., and Mao H. Facile synthesis and catalytic performance of Fe-containing silica-pillared clay derivatives with ordered interlayer mesoporous structure. Industrial & Engineering Chemistry Research. 2012; 51 (48): 15593–15600. https://doi.org/10.1021/ie3021413.

32. Jia Z., Peng K., and Xu L. Preparation, characterization and enhanced adsorption performance for Cr (VI) of mesoporous NiFe 2 O 4 by twice pore-forming method. Materials Chemistry and Physics. 2012; 136 (2): 512–519. https://doi.org/10.1016/j.matchemphys.2012.07.019.

33. Zhang J., Li B., Yang W., and Liu J. Synthesis of magnetic Fe_3O_4@hierarchical hollow silica nanospheres for efficient removal of methylene blue from aqueous solutions. Industrial & Engineering Chemistry Research. 2014; 53 (26): 10629–10636. https://doi.org/10.1021/ie5000533.

34. Malkoc E. Ni (II) removal from aqueous solutions using cone biomass of Thuja orientalis. Journal of hazardous materials. 2006; 137 (2): 899–908. https://doi.org/10.1016/j.jhazmat.2006.03.004.

35. Ho Y.-S. and McKay G. Sorption of dyes and copper ions onto biosorbents. Process Biochemistry. 2003; 38 (7): 1047–1061. https://doi.org/10.1016/S0032-9592(02)00239-X.

36. Del Bubba M., Arias C., and Brix H. Phosphorus adsorption maximum of sands for use as media in subsurface flow constructed reed beds as measured by the Langmuir isotherm. Water Research. 2003; 37 (14): 3390–3400. https://doi.org/10.1016/S0043-1354(03)00231-8.

37. Ng C., Losso J. N., Marshall W. E., and Rao R. M. Freundlich adsorption isotherms of agricultural by-product-based powdered activated carbons in a geosmin–water system. Bioresource technology. 2002; 85 (2): 131–135. https://doi.org/10.1016/S0960-8524(02)00093-7.

38. Wei Z., Xing R., Zhang X., Liu S., Yu H., et al. Facile template-free fabrication of hollow nestlike α-Fe_2O_3 nanostructures for water treatment. ACS applied materials & interfaces. 2012; 5 (3): 598–604. https://doi.org/10.1021/am301950k.

39. Yang L., Zhang Y., Liu X., Jiang X., Zhang Z., et al. The investigation of synergistic and competitive interaction between dye congo red and methyl blue on magnetic $MnFe_2O_4$. Chemical Engineering Journal. 2014; 246: 88–96. https://doi.org/10.1016/j.cej.2014.02.044.

40. Du Q., Sun J., Li Y., Yang X., Wang X., et al. Highly enhanced adsorption of congo red onto graphene oxide/chitosan fibers by wet-chemical etching off silica nanoparticles. Chemical Engineering Journal. 2014; 245: 99–106. https://doi.org/10.1016/j.cej.2014.02.006.

41. Ahmadi K., Ghaedi M., and Ansari A. Comparison of nickel doped Zinc Sulfide and/or palladium nanoparticle loaded on activated carbon as efficient adsorbents for kinetic and equilibrium study of removal of Congo Red dye. Spectrochimica Acta Part A: Molecular and Biomolecular Spectroscopy. 2015; 136: 1441–1449. https://doi.org/10.1016/j.saa.2014.10.034.

42. Lan S., Liu L., Li R., Leng Z., and Gan S. Hierarchical hollow structure ZnO: synthesis, characterization, and highly efficient adsorption/photocatalysis toward Congo red. Industrial & Engineering Chemistry Research. 2014; 53 (8): 3131–3139. https://doi.org/10.1021/ie404053m.